Thermal expansion of troilite and pyrrhotite determined by *in situ* cooling (873 to 373 K) neutron powder diffraction measurements

C. TENAILLEAU[1], B. ETSCHMANN[1], H. WANG[1], A. PRING[1,2,*], B. A. GRGURIC[3] AND A. STUDER[4]

[1] Mineralogy Department, South Australian Museum, North Terrace, Adelaide, S.A. 5000, Australia
[2] Department of Geology and Geophysics, University of Adelaide, North Terrace, Adelaide, S.A. 5005, Australia
[3] Exploration Group, WMC Resources Ltd, P.O. Box 91, Belmont, W.A. 6984, Australia
[4] Physics Division, ANSTO, PMB 1 Menai, N.S.W. 2234, Australia

The thermal expansion coefficients for natural troilite, FeS, Ni-rich pyrrhotite, $Fe_{0.84}Ni_{0.11}S$, and Ni-poor pyrrhotite, $Fe_{0.87}Ni_{0.02}S$, were measured during cooling by *in situ* neutron powder diffraction over the temperature range 873−373 K. Between 873 and 573 K, the mean thermal expansion coefficients for the three compositions are $7.4(3) \times 10^{-5}$ {FeS}, $8.0(4) \times 10^{-5}$ $\{Fe_{0.84}Ni_{0.11}S\}$ and $8.5(4) \times 10^{-5}$ K^{-1} $\{Fe_{0.87}Ni_{0.02}S\}$. Below 573 down to 373 K, the first two increase considerably to $14.1(7) \times 10^{-5}$ {FeS} and $9.3(5) \times 10^{-5}$ $\{Fe_{0.84}Ni_{0.11}S\}$ while the latter sample shows no significant variation, $8.4(5) \times 10^{-5}$ K^{-1}. Below 573 K, the thermal expansion is highly anisotropic, with $\Delta a/100$ K^{-1} ranging from 0.89(9)% {FeS} to 0.48(12)% $\{Fe_{0.87}Ni_{0.02}S\}$ while $\Delta c/100$ K^{-1} ranges from −0.39(11)% {FeS} to −0.13(2)% $\{Fe_{0.87}Ni_{0.02}S\}$.

Upon cooling through 573 K, troilite and pyrrhotite undergo a transition where the FeS_6 octahedra distort and in the case of pyrrhotite, cation-vacancy clustering occurs. The thermal expansion coefficients are bigger for low cation-vacancy concentrations and decrease as the pyrrhotites become less stoichiometric. This indicates that the thermal expansion in these minerals is damped by vacancy ordering or clustering. The thermal expansion coefficients for troilite and pyrrhotite are amongst the largest reported for sulphide minerals and their role in the formation of ore textures is discussed briefly.

KEYWORDS: thermal expansion, troilite, pyrrhotite, α and β transitions, neutron powder diffraction.

Introduction

PYRRHOTITE is the usual name given to the family of minerals with the general formula $Fe_{1-x}S$, where x is in the range 0 to 0.125. Pyrrhotite is an important mineral in many base metal sulphides deposits; particularly in primary ultramafic nickel sulphide deposits where it is invariably associated with pentlandite $(Fe,Ni)_9S_8$. In these ultramafic deposits the sulphide forms as an immiscible melt and upon cooling crystallizes as a single phase, the monosulphide solid solution (mss), the composition of which spans a wide range of Fe-Ni-sulphides, and has the NiAs structure. Upon cooling below 873 K, mss breaks down to form an intergrowth of pentlandite and pyrrhotite. Understanding the thermal behaviour of pentlandite and pyrrhotite is important in understanding the textures observed in natural ores.

All pyrrhotite structures can be derived from the simple hexagonal NiAs structure with a variety of superstructures associated with particular stoichiometries. The extremes are hexagonal troilite, the stoichiometric composition FeS, and monoclinic pyrrhotite for $x = 0.125$ (Fe_7S_8). The NiAs structure type consists of a hexagonal close-packed anion array with cations in the octahedral holes. The cation centred octahedra share faces

perpendicular to the hexagonal c repeat. This results in relatively short cation−cation distances. The ideal NiAs structure has space group $P6_3/mmc$ and for pyrrhotite compositions the subcell dimensions are $a \approx 3.4$ Å and $c \approx 5.9$ Å. The subcell structure contains only single Fe and S sites and all the Fe−S bonds are symmetrically equivalent and ~2.5 Å long.

The stoichiometric end-member, troilite, has a two-layer structure with no Fe vacancies and a 3A, 2C cell (where A and C refer to the a and c parameters of the parent NiAs subcell), in space group $P\bar{6}2c$ at ambient pressures and temperatures (Hägg, and Sucksdorff, 1933; King and Prewitt, 1982). Stoichiometric troilite is not a common mineral in terrestrial rocks, but is widely found in meteorites. Troilite undergoes two phase transitions in the temperature interval 380 to 600 K. The α transition, which occurs at ~413 K upon heating, is associated with magnetic moment spin-flip from perpendicular to parallel to the c axis; the second transition, at ~598 K, the so-called β transition, is associated with the antiferromagnetic to paramagnetic transition and corresponds to the transformation into the simple NiAs-like hexagonal subcell (space group $P63/mmc$) (Schwarz and Vaughan, 1972; Keller-Besrest and Collin, 1990*a*,*b*). Hägg and Sucksdorff (1933) noted the regular contraction of cell volume with decreasing Fe stoichiometry and were the first to propose the existence of Fe vacancies.

Natural monoclinic pyrrhotite ($Fe_{0.875}S$) contains 12.5% cation vacancies and these are ordered over a 4 layer structure with a 2A, $2\sqrt{3}$A, 4C cell (space group $C2/c$) and is ferrimagnetic (Tokonami *et al*., 1972). Fleet (1971) reported a trigonal 2A, 3C synthetic pyrrhotite $Fe_{0.875}S$, which has not been found in nature. 'Hexagonal' pyrrhotites ($Fe_{0.917}S$ to $Fe_{0.9}S$), are ordered intergrowths of full and vacancy-bearing layers with 5, 6, 7 or 11 layer repeats with 2A, nC cells with n equal to the number of stacking sequence (Morimoto *et al*., 1975*a*; Posfai and Dodony, 1990). Vacancy disorder within the layers is also possible and these phases are usually referred as 'nA pyrrhotite' (see Nakazama and Morimoto, 1971).

Above the β transition, pyrrhotite has the hexagonal subcell structure (Haraldsen, 1941), but upon cooling vacancy ordering in the metal lattice occurs, leading to the range of superstructures found in nature.

The two pyrrhotites studied here have some Ni substituted for Fe in the structures. Misra and Fleet (1973) studied the effects of Ni substitution into $Fe_{1-x}S$, and proposed that variation in the a parameter of the parent cell is largely controlled by the S lattice while the c parameter evolution is controlled by the metal content.

The data for the Ni-rich pyrrhotite described in this paper result from our study into the kinetics of the exsolution of pentlandite from mss/pyrrhotite using *in situ* cooling neutron powder diffraction (Etschmann *et al*., 2004). The sample originally consisted of an intergrowth of pentlandite and pyrrhotite that was homogenized at 973 K. It did not re-exsolve pentlandite during our cooling experiments, but during examination of the data we noted the unusual thermal expansion behaviour of pyrrhotite. This prompted a wider investigation of the variation of thermal expansion with composition in this system. The kinetic data are presented elsewhere (Etschmann *et al*., 2004; Wang *et al*., 2005). The main purpose of this paper is not to resolve the crystallographic and magnetic structures of those materials but to determine the variation of thermal expansion coefficients with composition and to see if this is linked to vacancy ordering and ore textures in these minerals.

The thermal expansion coefficients of a mineral are fundamental quantities related to strains introduced into the structure by changes in temperature. The thermal expansion coefficient, α, describing the volume change due to temperature variation, is generally defined by

$$\alpha = 1/VTr(dV/dT) \quad (1)$$

where Tr is the reference temperature (usually the lowest temperature in the thermal range considered) and VTr is the cell volume at the chosen reference temperature.

For cell volume data measured above room temperature the relationship to the thermal expansion is also expressed by

$$V(T) = VTr\exp[\int_{Tr}^{T}\alpha(T)dT] \quad (2)$$

Fei (1995) noted that when a thermal expansion coefficient is independent of temperature over the measured temperature range then

$$V(T) = VTr\exp[\alpha_o(T - Tr)] \quad (3)$$

The commonly used mean thermal expansion coefficient α_{mean} can be related to equation 2 by truncating the exponential series of $\exp[\alpha_o(T - Tr)]$ at its second order, i.e.

$$V(T) = VTr\ [1 + \alpha_{mean}(T - Tr)] \quad (4)$$

The extensive compilation of thermal expansion coefficient data for rock-forming minerals presented by Fei (1995) did not include those for the natural pyrrhotites reported earlier by Taylor (1970) and Tsatis (1988) up to 600 K. The latter authors related the anisotropy in the thermal expansion observed in pyrrhotite to the variations of the cation distances along the *c* axis and in the basal plane with temperature. In this paper we present the thermal expansion coefficients for troilite and pyrrhotites between 373 and 873 K upon cooling.

Experimental

Three natural compositions were selected for their specific compositions and their relatively low levels of impurities: (1) troilite from the Alta Mine, Del Nostra, California, USA (South Australian Museum G4902); (2) Ni-poor pyrrhotite from Sudbury, Ontario, Canada (South Australian Museum G543); and (3) Ni-rich pyrrhotite (originally an intergrowth of pyrrhotite and pentlandite that was homogenized by heating to 973 K) from Rocky's Reward Mine, Leinster, Western Australia (South Australian Museum G27920). Compositional data for these specimens are summarized in Table 1. The troilite and Ni-poor pyrrhotite can be considered as essentially pure FeS and Fe_7S_8, respectively. Around 4 g of each sample were crushed to an approximate average grain size of 0.1 mm (observed by optical microscope) and sealed under vacuum in 10 mm diameter Spectrasil tubes with a wall thickness of 0.25 mm. These sample tubes were loaded in vanadium cans before inserting into the furnaces.

The Ni-rich pyrrhotite was measured as part of a series of experiments investigating the kinetics of exsolution of pentlandite from mss (Etschmann *et al*. 2004) at ISIS and the heating and cooling regimes were designed to optimize the data for the kinetic study. The failure of the Ni-rich pyrrhotite sample to exsolve pentlandite upon cooling revealed the interesting thermal expansion behaviour of pyrrhotite and prompted this wider study. Unfortunately additional beam time at ISIS was not available to run the two other compositions so data were obtained on the medium-resolution powder diffractometer (MRPD) at Lucas Heights. The neutron beam intensity and resolution of the MRPD are considerably lower than for the HRPD at ISIS, so exactly the same experimental regime could not be used. The experimental protocols for the Lucas Heights experiments were optimized to give the best thermal expansion data and at the same time, to as far as was possible, mimic the cooling regime used at ISIS. The Ni-rich pyrrhotite sample had 5 wt.% Si added as an internal phase standard, but Si was not added to the other two samples as a phase standard was not necessary for the cell-parameter refinement. In spite of the different experimental protocols, the analysed data are consistent with each other and permit a comparison of unit-cell variation and thermal expansion evolution between all three-sample compositions.

TABLE 1. Summary of compositional data for natural troilite and pyrrhotites.

Mineral	S (wt.%)	Fe (wt.%)	Ni (wt.%)	Others (wt.%)
Troilite[1] (G4902)	34.8	61.0	0.0	4.2
Ni-rich pyrrhotite[2] (G27920)	36.0	52.8	7.7	3.5
Ni-poor pyrrhotite[3] (G543)	38.7	58.8	<1.2	n.det.

South Australian Museum registration numbers are given in brackets.

[1] From ICP digested sample measurements (Thomas *et al*., 2001). The Fe:S mole ratio was calculated to be 1.0:1.0.
The other elements detected (wt.%) include: Cu (0.16) and Si as SiO_2 (0.70). XRD powder measurements and an X-ray photoelectron spectroscopy survey of a polished surface of the troilite also revealed clinochlore $(Mg, Fe, Al)_6(Si, Cr)_4O_{10}(OH)_8$ (Thomas *et al*., 2003).

[2] From X-ray fluorescence measurements. Composition: $Fe_{0.84}Ni_{0.11}S$.
The other elements detected (wt.%) are: Mg as MgO (0.20), Co (0.14), Cu (0.17), Al as Al_2O_3 (0.10), Ca as CaO (0.70), Si as SiO_2 (1.40), As (39 ppm) and Cl (695 ppm).

[3] From microprobe analysis. This gives $Fe_{0.87}Ni_{0.02}S$, a composition very close to a pure end-member pyrrhotite $Fe_{0.875}S$.

Neutron diffraction at ISIS

In situ cooling (873 to 373±2 K) neutron powder diffraction data for Ni-rich pyrrhotite was collected on the high-resolution powder diffractometer (HRPD) at ISIS, Rutherford Appleton laboratory, Oxfordshire, England (see Ibberson *et al*., 1992 for details). The sample was heated to 973 K and held at this temperature for an 1 h to ensure an homogeneous solid solution, i.e. all of the exsolved pentlandite and pyrite were resorbed. The sample was then cooled over 24 h and neutron diffraction patterns were collected every 50 K from 973 down to 373 K, with additional steps at 853, 598 and 548 K. The sample was held at specific temperatures for ~24 min before the data set was collected over 36 min. Complementary backscattering (ZnS scintillator, bank 1) and 90º (ZnS scintillator, bank 2) detectors were used that span 2θ ranges of 160−176º and 80−100º, with Ω (ster) of 0.41 and 0.70, and have $\Delta d/d$ resolutions of $\sim 4 \times 10^{-4}$ and $\sim 2 \times 10^{-3}$, respectively. The time-of-flight data, collected in the range 35−120 ms (corresponding to *d*-spacing range of 0.72−2.49 Å), was then normalized to the incident neutron spectrum and the background subtracted and detector efficiency correction made using the program VA_COR (Ibberson *et al.*, 1992). A binning size of 1 was used and no self-scattering and absorption corrections applied.

Neutron diffraction at ANSTO

Neutron diffraction patterns for troilite and Ni-poor pyrrhotite were collected on the medium resolution powder diffractometer (MRPD) at ANSTO, Lucas Heights, Australia. The diffractometer has 32×3He detectors, a sample-to-detector distance of 0.7 m, a Be filter, a monochromator built with eight Ge crystals providing a flux of 3.8×10^5 n cm^{-2} s^{-1}, a resolution of 2.1×10^5 n cm^{-2}s^{-1} and a beam size of 2 cm × 5 cm. The background, with no sample, is 0.1 Hz. The studied temperature range was 873 to 373±2 K in steps of 20 K using a P1100 furnace. The samples were cooled rapidly between each temperature and held for 1 h to ensure thermal equilibrium, before the diffraction pattern was recorded over a 1 h period. Preliminary powder patterns were recorded at room temperature and diffraction patterns were recorded on both the heating and cooling cycles. A wavelength of 1.6655 Å was used and data were collected over the range 4º<2θ<138º, with a step size of 0.1º, normalized to the incident neutron spectrum and background subtracted. No scattering or absorption factor was taken into account.

Data-fitting procedures

Room-temperature patterns for the samples revealed that they each consisted predominantly of a single superstructure, but there was evidence for the intergrowth of small amounts of other superstructures and magnetic forms. We found it impossible to reliably fully refine the room-temperature powder diffraction data to a single characterized superstructure phase or even a mixture of two or more forms. For this reason and because there are no data for the Ni-rich pyrrhotite on the heating cycle, we have limited our study to the data collected during cooling. Once heated above 873 K, all these Fe sulphides transformed to the simple hexagonal NiAs-type subcell. The Rietveld method was used to refine the cell parameters to entire neutron diffraction patterns using the program Rietica (Hunter, 1997).

Since all the atoms in the hexagonal pyrrhotite subcell occupy special positions within the unit cells, the Rietveld refinement was limited to refining the cell parameters and a limited number of profile parameters. These included the phase proportions, an overall thermal parameter, peak shape parameters (U, V and W from the FCJ asymmetric pseudo-Voigt function for the ANSTO data and sigma 1 from the Jorgensen-type function for the ISIS data) for each phase and six terms of a type I Chebyshev profile background function, that included the contribution to the pattern background from the silica sample tubes. The zero shift (and other gamma or beta peak shape parameters in the case of the ISIS data) were fixed all the way down to 373 K after being refined at the highest temperature. Only the atomic positions for the low-temperature troilite phase were then refined. No absorption or self-scattering corrections were applied. The atomic ratios were fixed following the general compositions and neutral scattering lengths were used in the models.

Results and discussion

The observed and calculated diffraction patterns for troilite at 293 K, together with the difference trace are shown in Fig. 1. The data set was

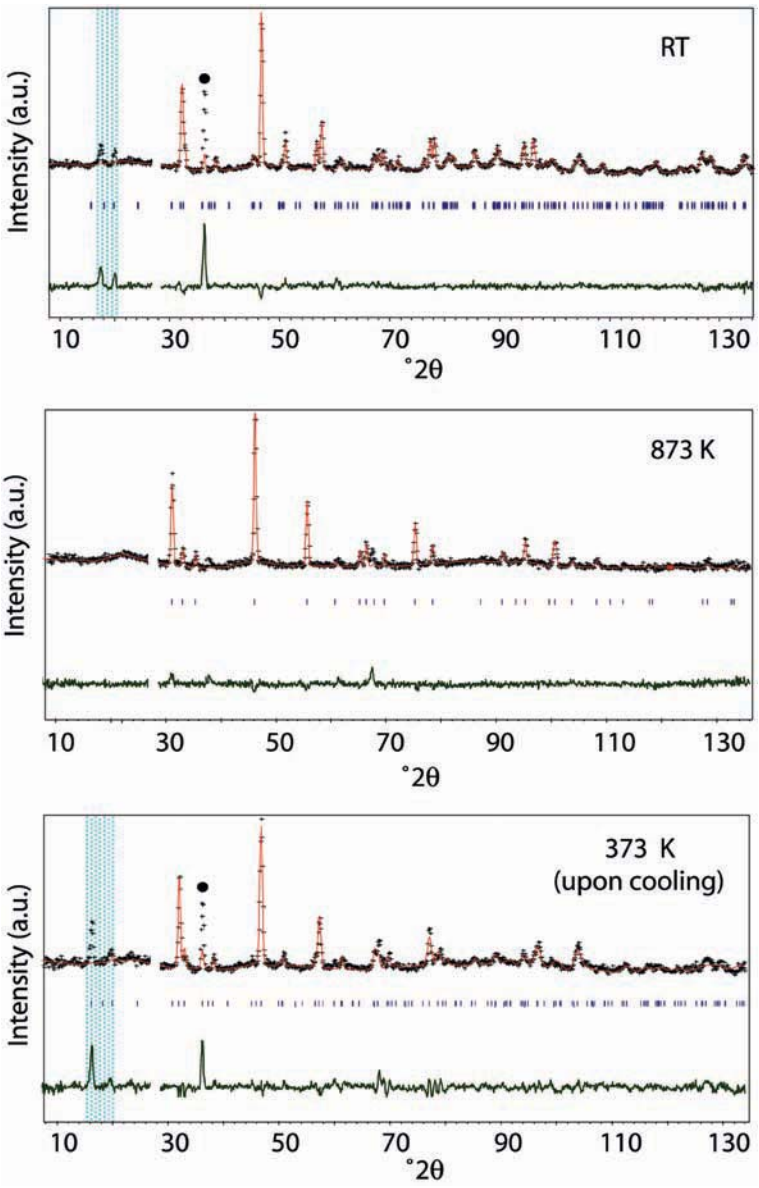

FIG. 1. Observed (cross) and calculated (weak line) neutron diffraction pattern for troilite together with a difference trace (strong line) at three different temperature: 293 K (upper), 873 K (middle) and 373 K (lower). Bragg peaks are represented by small vertical lines. The shaded regions cover regions excluded from the Rietveld refinements. The black dot indicates a $011_{subcell}$ reflection which fits poorly due to a magnetic contribution to reflection intensity which was not modelled in the refinement. Goodness-of-fit parameters (R_p, R_{wp}, R_{exp}, χ^2) are: 0.0424, 0.0743, 0.0317, 5.482 at 293 K; 0.0491, 0.0631, 0.0439, 2.065 at 873 K; and 0.0621, 0.0867, 0.0430, 4.062 at 373 K.

recorded before the sample was heated to 873 K. A room-temperature X-ray diffraction (XRD) study on the same sample by Thomas *et al*. (2003) found minor amounts of clinochlore $(Mg,Fe,Al)_6(Si,Cr)_4O_{10}(OH)_8$ and additional reflections attributed to an unknown phase. The first main reflections observed in the neutron diffraction patterns related to clinochlore at

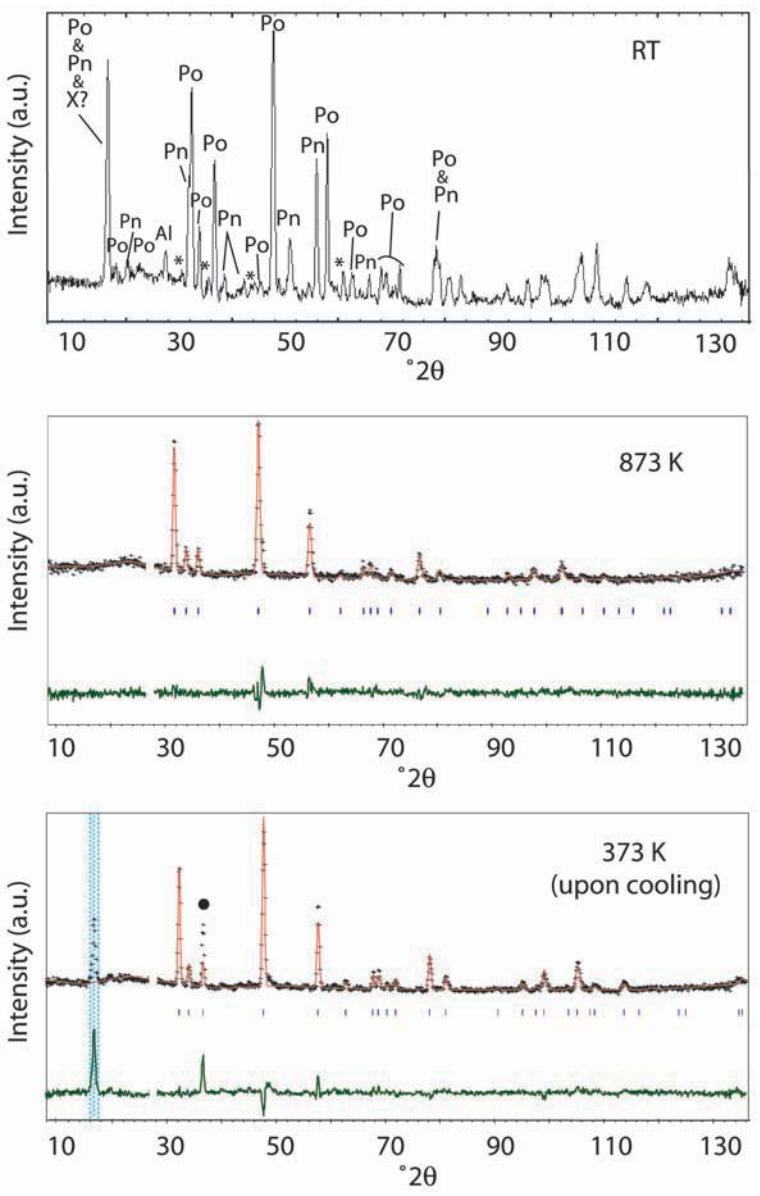

FIG. 2. Observed neutron diffraction pattern for the Ni-poor pyrrhotite at 293 K (upper). The main reflections are identified as follows: Po for monoclinic pyrrhotite, Pn for pentlandite, a star symbol for a minor amount of pyrite and *Al* for the alumina coming from the experimental furnace used at ANSTO. Then, observed (cross), calculated (weak line) and difference (strong line) patterns of Ni-poor pyrrhotite at 873 K (middle) and 373 K (lower). Bragg peaks are indicated by small vertical lines. The shaded regions were excluded from the Rietveld refinements. The black dot indicates the $011_{subcell}$ reflection that also contains a magnetic contribution to its intensity. Goodness-of-fit parameters (R_p, R_{wp}, R_{exp}, χ^2) are: 0.0583, 0.0762, 0.0525, 2.110 at 873 K; and 0.0690, 0.0967, 0.0519, 3.473 at 373 K.

d = 4.84 Å (2θ = 9.8º) and the 'unidentified' phase at d = 5.50 Å (2θ = 17.4º) were excluded from our refinements. We believe that the reflection at d = 5.50 Å is probably a superlattice

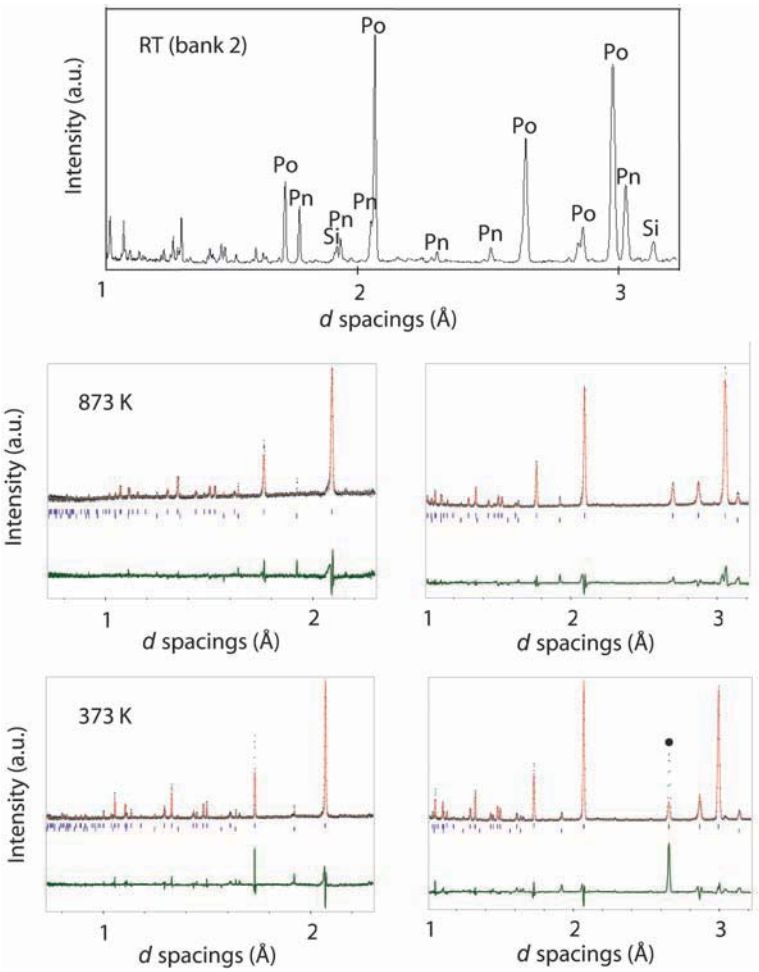

FIG. 3. Observed (upper) pattern for the Ni-rich pyrrhotite at room temperature. The first main peaks (greater *d* spacings) are identified as follows: Po for hexagonal pyrrhotite and Pn for pentlandite. *Si* corresponds to the silicon standard (~5 wt.%) added to the sample. Also, observed (cross), calculated (weak line) and difference (strong line) patterns for the Ni-rich pyrrhotite refinements at 873 K (middle) and 373 K (lower) from detector banks 1 and 2 (left to right). Bragg peaks are represented by small vertical lines (*Si* = bottom lines). For example, a_{Si} = 5.4428(4) and 5.4320(6) Å at 873 and 373 K, respectively, in good agreement with Dutta's data (1962). The black dot indicates the $011_{subcell}$ reflection that has a magnetic contribution to its intensity. Goodness-of-fit parameters (R_p, R_{wp}, R_{exp}, χ^2 (bank 1/bank 2)) are: 0.0661/0.0697, 0.0821/0.1012, 0.0533/0.0298, 2.374/11.513 at 873 K; and 0.0896/0.1222, 0.1210/0.1860, 0.0526/0.0285, 5.293/42.714 at 373 K.

reflection of FeS. The 293 K data set was then successfully refined to the 3A, 2C cell in space group $P\bar{6}2c$. Only the intensity of the $(011)_{subcell}$ reflection at 36.3º (d = 2.67 Å), could not be properly modelled by the refinement. This reflection has both a structural and magnetic contribution (due to partial antiferromagnetic ordering). Full characterization of this magnetic ordering is beyond the scope of the current work.

At 873 K the troilite pattern was refined on the simple hexagonal subcell ($a \approx 3.55$ and $c \approx 5.81$ Å and space group $P6_3/mmc$) (see Fig. 1). This structure was used successfully in refinements of all the data sets collected at temperatures down to 573 K. On cooling through 573 K the β transition occurs and this is also marked by the large increase in intensity of the $(011)_{subcell}$ line and the appearance of an extra reflection at d =

5.92 Å at this particular temperature. This line is not wholly associated with magnetic ordering as it also occurs in the XRD pattern. The magnetic contribution to $(011)_{subcell}$ reflection and the unassigned superlattice line (d = 5.92 Å at 573 K) progressively increase in intensity as the temperature decreases. Between 573 K and 373 K the diffraction data were refined on the 3A, 2C troilite superstructure (space group $P\bar{6}2c$) (see Fig. 1).

Using the compositional data presented in Table 1 and XRD data the main pyrrhotite polytypes present at room temperature were identified and are indicated on the neutron patterns for the Ni-poor and Ni-rich pyrrhotites in Figs 2 and 3, respectively.

The Ni-poor pyrrhotite consisted mainly of monoclinic pyrrhotite (Po), pentlandite (Pn) and a small amount of pyrite while the Ni-rich pyrrhotite was a mixture of hexagonal pyrrhotite(s) and pentlandite (see Figs 2 and 3). All the data sets recorded at temperatures between 873 and 373 K were refined on the simple pyrrhotite subcell in space group $P6_3/mmc$ with the metal-site occupancy factor fixed at the appropriate stoichiometric value (see Figs 2 and 3). Cooling of these pyrrhotite samples resulted in very similar patterns of behaviour to that of troilite,

TABLE 2. Cell parameters for troilite and pyrrhotites.

T	Troilite (G4902)			Ni- rich pyrrhotite (G27920)			Ni-poor pyrrhotite (G543)		
(K)	a (Å)	c (Å)	V (Å^3)	a (Å)	c (Å)	V (Å^3)	a (Å)	c (Å)	V (Å^3)
873	3.5538(4)	5.810(1)	63.55(3)	3.5297(1)	5.7460(2)	62.00(1)	3.5060(8)	5.688(1)	60.54(3)
853	3.5526(2)	5.807(1)	63.47(3)	3.5279(1)	5.7422(2)	61.89(1)	3.5031(7)	5.679(1)	60.36(3)
833	3.5511(2)	5.803(1)	63.38(3)				3.5013(6)	5.676(1)	60.26(3)
823				3.5252(1)	5.7370(2)	61.74(1)			
813	3.5496(2)	5.801(1)	63.30(3)				3.4984(6)	5.671(1)	60.10(3)
793	3.5478(2)	5.798(1)	63.20(3)				3.4982(6)	5.668(1)	60.07(3)
773	3.5462(2)	5.796(1)	63.12(3)	3.5209(1)	5.7295(2)	61.51(1)	3.4952(6)	5.665(1)	59.94(3)
753	3.5444(2)	5.794(1)	63.04(3)				3.4926(6)	5.662(1)	59.82(3)
733	3.5431(2)	5.790(1)	62.95(3)				3.4921(6)	5.661(1)	59.78(3)
723				3.5164(1)	5.7227(1)	61.28(1)			
713	3.5413(2)	5.788(1)	62.86(3)				3.4906(6)	5.658(1)	59.72(3)
693	3.5392(2)	5.785(1)	62.76(3)				3.4888(6)	5.655(1)	59.61(3)
673	3.5376(2)	5.784(1)	62.69(3)	3.5117(1)	5.7166(1)	61.05(1)	3.4870(6)	5.652(1)	59.52(3)
653	3.5357(2)	5.782(1)	62.60(3)				3.4856(6)	5.652(1)	59.47(3)
633	3.5333(2)	5.780(1)	62.49(3)				3.4846(5)	5.652(1)	59.44(3)
623				3.5062(1)	5.7122(1)	60.81(1)			
613	3.5308(2)	5.779(1)	62.39(3)				3.4814(5)	5.648(1)	59.28(3)
598				3.5029(1)	5.7109(1)	60.69(1)			
593	3.5279(2)	5.778(1)	62.28(3)				3.4793(5)	5.648(1)	59.22(3)
573	3.5246(2)	5.778(1)	62.16(3)	3.4983(1)	5.7133(1)	60.55(1)	3.4751(5)	5.645(1)	59.04(3)
553	3.5182(2)	5.783(1)	61.99(3)				3.4689(5)	5.644(1)	58.81(3)
548				3.4923(1)	5.7193(1)	60.41(1)			
533	3.5119(2)	5.787(1)	61.81(3)				3.4634(5)	5.647(1)	58.66(3)
523				3.4869(1)	5.7237(1)	60.27(1)			
513	3.5065(2)	5.790(1)	61.65(3)				3.4612(5)	5.650(1)	58.62(3)
493	3.5014(2)	5.793(1)	61.51(3)				3.4567(5)	5.650(1)	58.47(3)
473	3.4967(2)	5.795(1)	61.36(3)	3.4772(1)	5.7292(1)	59.99(1)	3.4541(5)	5.653(1)	58.41(3)
453	3.4922(3)	5.798(1)	61.23(3)				3.4516(5)	5.656(1)	58.35(3)
433	3.4875(3)	5.799(1)	61.08(3)				3.4489(5)	5.657(1)	58.27(3)
423				3.4683(1)	5.7328(1)	59.72(1)			
413	3.4823(3)	5.802(1)	60.93(3)				3.4465(5)	5.656(1)	58.18(3)
393	3.4781(3)	5.804(1)	60.81(3)				3.4444(5)	5.657(1)	58.13(3)
373	3.4623(3)	5.824(2)	60.45(1)	3.4596(1)	5.7341(2)	59.44(1)	3.4417(5)	5.660(1)	58.06(3)

The standard deviations are given in brackets after the cell parameters.

with the $(011)_{subcell}$ reflection becoming more intense as the temperature decreased below the β transition. Powell *et al*. (2004) recently showed that the change in intensity of the $(001)_{subcell}$ reflection monoclinic pyrrhotite Fe_7S_8 is associated with magnetic ordering below the β transition.

The overall quality of our neutron diffraction data was constrained by the relatively short data collection times. This is illustrated by the relatively poor fit for the silicon standard in the Ni-rich pyrrhotite data (see Fig. 3). However, these data are largely sufficient to follow the cell evolution with temperature.

The unit-cell parameters from 873 to 373 K for the three samples are summarized in Table 2 and

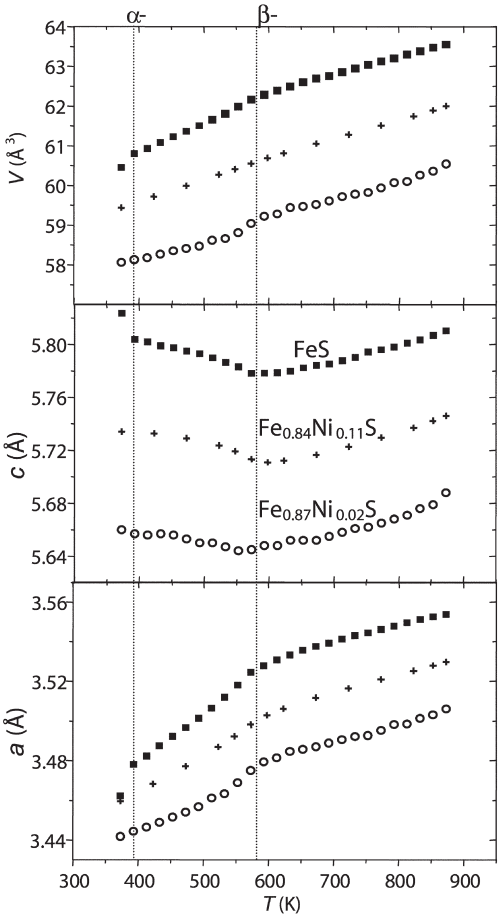

FIG. 4. Thermal evolution of cell parameters for troilite (square), Ni-rich pyrrhotite (cross) and Ni-poor pyrrhotite (open circle). The α and β transitions are indicated by vertical lines.

their thermal evolutions are shown in Fig. 4. Upon cooling, the β and α transitions, are marked by breaks in slope in the thermal evolution of the cell parameters at ~573 and 390 K, respectively. The *a* cell parameter decreases linearly from high temperature to the β-transition temperature and then decreases more rapidly below it for each sample. There appears to be an abrupt change in *a* that marks the α transition for troilite, but there is no such evidence for this transition in the Ni-rich and Ni-poor pyrrhotites. The *c* parameters for the three compositions also decrease, but non-linearly down to 573 K. All three samples undergo a contraction along both the *c* axis and in the basal plane of the hexagonal subcell before the β transition. Then *c* increases upon further cooling, with a marked change at the α-transition temperature in the case of troilite. Taylor (1970) also noted this negative thermal expansion along *c*, although his data were measured during heating rather than cooling. He explained the increase in *c* between the α and β transitions in terms of the onset of metal/vacancy ordering.

The volumes of all three samples decrease continuously over the whole thermal range studied. There is a change in slope at ~573 K, corresponding to the β transition. Below the transition temperature the volume decrease is amplified due to the strong contraction in the basal plane of the hexagonal subcell. This contraction is much larger than the relaxation along the *c* axis. Only troilite shows a distinct break in slope at 390 K due to the α transition. Keller-Besrest and Collin (1990*a*,*b*) explained the α transition in troilite using a polaron mechanism and noted that it is suppressed for high *x* values in $Fe_{1-x}S$. Our results are consistent with the α transition being suppressed as the cation vacancy concentration increases. Note also that the cell volume decreases as *x* increases, but the transition temperature does not change significantly with Fe stoichiometry. The fact that both β- and α-transition temperatures are lower than those reported for troilite (598 and 413 K, respectively) (Schwarz and Vaughan, 1972; Keller-Besrest and Collin, 1990*a*,*b*), is due to hysteresis between cooling and heating experiments.

The thermal expansion coefficients, determined using equation 1, for the three samples examined here upon cooling, together with the data from Taylor (1970), including those from metastable and monoclinic pyrrhotite, are summarized in Table 3. Between 873 and 573 K, the mean thermal expansion coefficients vary from

TABLE 3. Thermal expansion data for troilite and pyrrhotites from *in situ* cooling experiments and comparison with literature.

Sample	Temp. range (K)	Thermal exp. α (*10^{-5} K^{-1})	Δ*a*/100 K[#] %	Δ*c*/100 K[#] %
FeS	873−573	7.4(3)	0.29(7)	0.18(7)
	573−373	14.1(7)	0.89(9)	−0.39(11)
$Fe_{0.84}Ni_{0.11}S$	893−573	8.0(4)	0.31(7)	0.19(10)
	573−373	9.3(5)	0.56(5)	−0.18(10)
$Fe_{0.87}Ni_{0.02}S$	893−573	8.5(4)	0.32(3)	0.26(14)
	573−373	8.4(5)	0.48(12)	−0.13(2)
FeS*	593−723	7.2	0.28	−0.04
	413−593	12.5	0.84	−0.37
$Fe_{0.961}S$*	593−723	6.1	0.30	−0.05
	388−593	11.6	0.67	−0.24
$Fe_{0.923}S$*	593−723	6.9	0.34	−0.02
	348−593	12.6	0.70	−0.17
$Fe_{0.875}S$*	565−593	~8	0.43	−0.22
	298−565	9.0	0.54	~0

* From Taylor (1970). Data for the sample $Fe_{0.875}S$ in the upper temperature range actually refer to the monoclinic cell and in the lower range to a metastable hexagonal pyrrhotite.
[#] Average % $\Delta p/100\ K = \Delta p \times (100/p_0) \times 100$ K, where p is the cell parameter (a or c) and p_0 the value at the lowest temperature in the considered temperature range. Here, the uncertainties indicated into brackets correspond to the difference between the average value and the maximum or minimum value determined over 100 K in the considered range.

7.4×10^{-5} (FeS) to 8.5×10^{-5} K^{-1} ($Fe_{0.87}Ni_{0.02}S$) and between 573 and 373 K, they increase considerably for $Fe_{0.84}Ni_{0.11}S$ (9.3×10^{-5} K^{-1}) and FeS (14.1×10^{-5} K^{-1}) while the value for $Fe_{0.87}Ni_{0.02}S$ does not change significantly (8.4×10^{-5} K^{-1}), despite being calculated over a temperature range smaller by 100 K. Thus, overall α is significantly higher below the β transition than at temperatures above. The thermal expansion coefficient α increases with increasing metal concentration below the β-transition temperature, while above this temperature, it decreases slightly. These trends are less evident in Taylor's (1970) data (Table 3); however, there is generally good agreement between the two sets of thermal coefficients.

The values of Δ*a*/100 K show a similar tend, increasing with metal concentration below the β transition but showing little variation above. The magnitude of the negative value of Δ*c*/100 K increases with increasing metal concentration below the β-transition temperature. Above this transition temperature, our data show that Δ*c*/100 K tends to decrease as the compositions become closer to stoichiometry.

The thermal expansion coefficients of these Fe sulphides are amongst the largest reported for sulphide minerals. The thermal expansion for troilite below the β transition is similar to that of cubic pentlandite (13.4×10^{-5} K^{-1}) over the 298−873 K temperature range (Sugaki and Kitakaze, 1998) but the thermal expansion is somewhat smaller for non-stochiometric pyrrhotites. The large thermal expansion in pentlandite was attributed to order-disorder of metal atoms between non-equivalent sites and spin-state changes (Rajamani and Prewitt, 1975). However, it would appear that the high thermal expansion of Fe-rich pentlandites is associated with the accommodation of interstitial metal ions or S vacancies as Ni-rich pentlandites show cation deficiency $(Ni,Fe)_{9-x}S_8$ and Fe-rich pentlandites have cation excess $(Fe,Ni)_{9+x}S_8$ (Vaughan and Craig, 1978).

The differential in thermal expansion behaviour between pyrrhotite and Fe-rich pentlandite is significant from the point of view of natural ore textures, particularly those in massive magmatic nickel sulphide ores. In such ores, pentlandite (Ni content 33−36 wt.%) typically occurs as exsolved bodies of various morphologies in more voluminous monoclinic pyrrhotite (Kelly

and Vaughan, 1983; Roberts and Travis, 1986). The nickel content of pyrrhotites in these ores is typically 0.3–0.6 wt.%. Cooling deposition results in the development of distinctive fracturing in pentlandite bodies, due to their higher expansion coefficient (contraction) relative to the host pyrrhotite. The fractures typically correspond with {111} cleavage planes and markedly increase the permeability and susceptibility of these ores to supergene alteration fluids. In addition, the development of microfractures in pentlandite results in a higher degree of fragility in this mineral during grinding of massive sulphide ores as a prelude to froth flotation mineral processing. Over-grinding and possible reduced Ni recoveries are a consequence. On the other hand, these microfractures assist in the liberation of pentlandite particles from enclosing pyrrhotite, magnetite or silicate minerals.

Acknowledgements

We wish to thank Kevin Knight of Rutherford Appleton Laboratory and Andrew Putnis for their assistance with data collection. We are very grateful to the referee(s) of the earlier version who prompted us with very pertinent comments that helped considerably to present our results in a more logical fashion. We acknowledge the financial assistance of the Australian Research Council and the Australian Institute for Nuclear Science and Engineering.

References

Dutta, B.N. (1962) Lattice constants and thermal expansion of silicon up to 900C. *Physical Status Solidi*, **2**, 984–987.

Etschmann, B.E, Pring, A., Putnis, A., Grguric, B.A. and Struder, A. (2004) A kinetic study of the exsolution of pentlandite $(Ni,Fe)_9S_8$ from the monosulphide solid solution (Fe,Ni)S. *American Mineralogist*, **89**, 39–50.

Fei, Y. (1995) Thermal Expansion (extract from: *Mineral Physics and Crystallography*; *A handbook of Physical Constants,* T.J. Ahrens, editor). American Geophysical Union Reference Shelf, **2**, pp. 29–44.

Fleet, M.E. (1971) The crystal structure of a pyrrhotite (Fe_7S_8). *Acta Crystallographica*, **B27**, 1864–1867.

Hägg, G. and Sucksdorff, I. (1933) Die kristallstruktur von troilit und magnetkies. *Zeitschrift fur Physikal Chemie*, **B22**, 444–452.

Haraldsen, H. (1941) Uber die eisen(II)-sulfidmischkristalle. *Zeitschrift für Angoranische Chemie*, **246**, 195–226.

Hunter, B.A. (1997) *IUCr Powder Diffraction 22, 21. Rietica 1.7.7.* Rietveld Analysis Program.

Ibberson, R.M., David, W.I.F. and Knight, K.S. (1992) *The High Resolution Neutron Powder Diffractometer (HRPD) at ISIS – A User Guide.* Report RAL-92-031.

Keller-Besrest, F. and Collin, G. (1990*a*) Structural aspects of the α-transition in stoichiometric FeS: Identification of the high-temperature phase. *Journal of Solid State Chemistry*, **84**, 194–210.

Keller-Besrest, F. and Collin, G. (1990*b*) Structural aspects of the α-transition in off-stoichiometric $Fe_{1-x}S$ crystals. *Journal of Solid State Chemistry*, **84**, 211–225.

Kelly, D.P. and Vaughan, D.J. (1983) Pyrrhotine-pentlandite ore textures: a mechanistic approach. *Mineralogical Magazine*, **47**, 453–463.

King, H.E. and Prewitt, C.T. (1982) High-pressure and high-temperature polymorphism of iron sulphide (FeS). *Acta Crystallographica*, **B38**, 1877–1887.

Misra, K.C. and Fleet, M.E. (1973) Unit cell parameters of monosulphide, pentlandite and taenite solid solutions within the Fe-Ni-S system. *Materials Research Bulletin*, **8**, 669–678.

Morimoto, N., Gyobu, A., Tsukuma, K. and Koto, K. (1975*a*) Superstructure and nonstoichiometry of intermediate pyrrhotite. *American Mineralogist*, **60**, 240–248.

Morimoto, N., Gyobu, A., Mukaiyama, H. and Izawa, E. (1975*b*) Crystallography and stability of pyrrhotites. *Economic Geology*, **70**, 824–833.

Nakazama, H. and Morimoto, N. (1971) Phase relations and superstructures of pyrrhotite, $Fe_{1-x}S$. *Materials Research Bulletin*, **6**, 345–358.

Pósfai, M. and Dódony, I. (1990) Pyrrhotite superstructures. Part I: Fundamental structures of the NC (N=2, 3, 4 and 5) type. *European Journal of Mineralogy*, **2**, 525–528.

Powell, A.V., Vaqueiro, P., Knight, K.S., Chapon, L.C. and Sanchez, R.D. (2004) Structure and magnetism in synthetic pyrrhotite Fe_7S_8: A powder neutron-diffraction study. *Physical Review B (Condensed Matter and Materials Physics - 1)*, **70**, 014415.

Rajamani, V. and Prewitt, C.T. (1975) Thermal expansion of the pentlandite structure. *American Mineralogist*, **60**, 39–48.

Roberts, D.E. and Travis, G.A. (1986) Microtextural evaluation of nickel sulphide gossans in Western Australia. *Transaction of the Royal Society of Edinburgh: Earth Sciences*, **77**, 81–98.

Schwarz, E.J. and Vaughan, D.J. (1972) Magnetic phase relations of pyrrhotite. *Journal of Geomagnetism and Geoelectricity,* **24**, 441–458.

Sugaki, A. and Kitakaze, A. (1998) High form of pentlandite and its thermal stability. *American Mineralogist*, **83**, 133–140.

Taylor, L.A. (1970) Low temperature phase relations in the Fe-S system. *Carnegie Institute of Washington Year Book*, **68**, 259−267.

Thomas, J.E., Skinner, W.M. and Smart R.St.C. (2001) A mechanism to explain sudden changes in rates and products for pyrrhotite dissolution in acid solution *Geochimica et Cosmochimica Acta*, **65**, 1−12.

Thomas, J.E., Skinner, W.M. and Smart R.St.C. (2003) A comparison of the dissolution behavior of troilite with other iron(II) sulfides; implications of structure. *Geochimica et Cosmochimica Acta*, **67**, 831−843.

Tokonami, M., Nishiguchi, K. and Morimoto, N. (1972) Crystal structure of a monoclinic pyrrhotite (Fe_7S_8). *American Mineralogist*, **37**, 1066−1080.

Tsatis, D.E. (1988) Thermal expansion of pyrrhotite (Fe_7S_8) at high temperatures. *Journal of Physics and Chemistry of Solids*, **49**, 359−362.

Vaughan, D.J. and Craig, J.R. (1978) *Mineral Chemistry of Metal Sulphides*. Cambridge University Press, Cambridge, UK, 493 pp.

Wang, H., Pring, A., Ngothai, Y. and O'Neill, B. (2005) A low temperature kinetic study of the exsolution of pentlandite from the monosulfide solid solution using a refined Avrami equation. *Geochimica et Cosmochimica Acta,* **69**, 415−425.